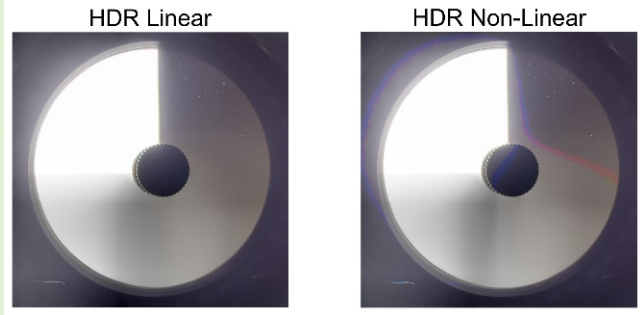


Method for Evaluation of Linearity of Image Sensors in High Dynamic Range Mode

Orit Skorka^{ID}, Member, IEEE, Barry Vanhoff^{ID}, Rujul Desai, and Radu Ispasoiu

Abstract—Image sensors in cameras that are used for outdoor imaging, such as for automotive applications, are typically operated in the high dynamic range (HDR) mode. Photo-response linearity is a key performance indicator of image sensors. Existing procedures for the evaluation of image sensor linearity are based on exposure variation. They are efficient when image sensors are operated in the basic mode, which has a limited dynamic range (DR), however, they are difficult or impractical to implement with image sensors in the HDR mode. This work presents a method to evaluate the linearity of image sensors in the HDR mode. The method uses an indirect approach, which is based on the relative response between color channels in color cameras. It is independent of the HDR mechanism and the actual photo-response ratios between color channels; it can be applied to monochrome cameras with attenuation filters. We demonstrate the method with a camera module that includes a color image sensor that is activated in the HDR mode with the recommended configuration file and with a file that was modified to produce a nonlinear HDR response. Raw image data were collected with test targets in a controlled laboratory environment and outdoors in a representative HDR scene. The data were used to calculate signal and noise properties to construct the signal-to-noise ratio and relative channel response curves and to evaluate color properties. Analysis of the relative response curves shows that the proposed method is highly sensitive to deviation from linearity and that it correlates well with color artifacts.

Index Terms—Automotive imaging, color artifacts, electronic imaging, high dynamic range (HDR), image sensor, linearity, signal-to-noise ratio (SNR).



I. INTRODUCTION

POTO-RESPONSE linearity is a key performance indicator of imaging systems, specifically, in applications that rely on absolute and relative contrast [1]. With color cameras, since color processing is based on linear operations, deviation from linearity can result in the appearance of color artifacts in the image after color processing. The European Machine Vision Association (EMVA) 1288 standard for the characterization of image sensors and cameras [2] includes a method for evaluation of linearity through variation of exposure, which is the product of image plane irradiance and integration time. With this method, exposure can be varied by a change in integration time, the light level of a continuous light source, or the duty cycle of a pulsed light source.

Manuscript received 2 March 2023; accepted 10 April 2023. Date of publication 18 April 2023; date of current version 31 May 2023. The associate editor coordinating the review of this article and approving it for publication was Ms. Shiva Abbaszadeh. (Corresponding author: Orit Skorka.)

Orit Skorka, Rujul Desai, and Radu Ispasoiu are with the Intelligent Sensing Group, onsemi, San Jose, CA 95134 USA (e-mail: Orit.Skorka@onsemi.com).

Barry Vanhoff is with the Intelligent Sensing Group, onsemi, Corvallis, OR 97333 USA.

Digital Object Identifier 10.1109/JSEN.2023.3267046

The intrascene dynamic range (DR) of an image sensor is the ratio between the brightest and darkest light levels that can be perceived in a single frame, and the scene DR is the illumination ratio between the brightest and darkest regions in the scene. The basic operating mode of most CMOS image sensors (CISs) is based on the integration of photo-charge during EXP time. In this mode, the sensor DR is typically lower than 75 dB. This value is insufficient for applications where the scene DR is high, for example, the DR of outdoor scenes can reach 120–140 dB [3]. Therefore, cameras that operate in high DR (HDR) environments rely on image sensors that are activated in the HDR mode. There are numerous approaches to achieve HDR response, such as nonlinear response, multi-EXP with varied integration time, varied gain, frame oversampling and photon counting, overflow capacitor, and multiple photo-sensing elements [4].

While exposure-based methods to evaluate linearity works well with sensors that are operated in the basic mode, they become very difficult or even impractical to implement with sensors that are operated in the HDR mode. In the HDR mode, variation of integration time can affect the sensor response curve, use of a pulsed light source may create flicker artifacts, and light sources that can cover a DR of 120–140 dB without

change in the spectrum and with high precision are very costly.

This work presents a method to evaluate the photo-response linearity of image sensors in the HDR mode. With color cameras, the method uses the relative response between color channels, and with monochrome cameras, the same method can be implemented with attenuation filters. This is advantageous as it allows us to overcome the possible factors of illumination nonlinearity, variations in illuminant spectrum with light level, and the effect of flare in the camera module that can lead to a nonlinear relationship between the source and image plane illumination. The method is robust and can be used with various types of HDR mechanisms. Data analysis considers interchannel derivatives of the photo-response signals, which show high sensitivity to deviation from linearity. A hidden assumption in this approach is that pixel performance is rather uniform across the array. This assumption is valid for state-of-the-art CIS as, although outlier pixels are unavoidable, their density is very low.

This article is organized as follows. Section II covers the methodology and presents results from the simulation of an image sensor in the HDR mode. Section III presents results from experimental work using images that were captured in a controlled laboratory environment and outdoors. Section IV discusses the correlation between deviation from linearity and color artifacts.

II. METHOD

To ensure that linearity is properly evaluated for the entire DR in the operating mode of the end-user application, the sensor signal-to-noise ratio (SNR) curve in this mode should be known to the user. In general, linearity is expected to be lower in very low signal levels and in signal levels that are close to saturation due to noise and imperfections of peripheral circuits. In the HDR mode, linearity may be degraded in signal levels around transition regions in the SNR curve. Section A describes the software tool that was developed and used to simulate the response of an image sensor in the HDR mode. Section B presents the proposed linearity metric and demonstrates the results with the simulated HDR response, and Section C shows results when the sensor HDR response is modified in a way that introduces nonlinearity.

A. HDR Mode Characteristics

Signal and noise simulations were done in MATLAB for a group of 400 pixels in the 3-exposure (3-EXP) HDR mode under 530-nm (green light) illumination when the junction temperature, T_j , that is, the temperature of the image sensor die, was 60 °C. In this operating mode, the HDR image is produced by combining three images that are captured consecutively with three integration times, T_1 , T_2 , and T_3 , where T_1 is the longest integration time, and T_3 is the shortest. To achieve a response of an image sensor with the common Bayer color filter array (CFA) pattern [5], the simulation was repeated for pixels with green (G), blue (B), and red (R) color filters.

Both dark-current and photo-current contribute to the charge that is accumulated in the pixel capacitance during the integration time. Mechanisms that contribute to the dark signal

TABLE I
PIXEL PARAMETERS USED IN SIMULATION

Parameter	Value	Comment
Quantum efficiency at 530 nm	11%, 83%, and 19%	Mean value for R, G, and B pixels, respectively
System gain	0.74 DN/e-	Mean value
Readout noise	2.8 e-	Root-mean-square value
Dark current	32 e-/s/pixels	Mean value
Integration time	15 ms, 0.64 ms, 0.04 ms	T_1 , T_2 , T_3 , respectively
Dark-signal non-uniformity (DSNU)	3 e-, 2 e-, 2 e-	For T_1 , T_2 , T_3 , respectively

depend on the concentration of trap states, electric field, and temperature. They include thermal generation in the photodiode and at interface locations, such as the transfer gate and trench insulations [6].

The spatial distribution of pixel parameters may be approximated by a Gaussian with an exponential tail [7], [8]. Therefore, the normal distribution model is suitable to use to describe variations among all pixels, excluding outliers, and this model was used to spatially vary parameters among the 400 pixels. To include the effect of temporal noise, 30 simulation runs were done for each pixel. Dark and photo-signals were varied around a mean value using shot-noise statistics which was implemented with the Poisson-noise model [9]. The Gaussian noise model was used to implement temporal variations of the thermal component of readout noise, where the effect of the small pixel population that is affected by random-telegraph signal (RTS) noise was not considered [10]. The total signal in charge units was converted to digital numbers (DNs) using mean system gain. Then mean dark signal of the 400 pixels was subtracted from the total signal of all pixels to obtain the photo-signal. Table I lists all parameters and their mean value, when applicable.

Fig. 1(a) presents the simulated mean photo-signal, μ , of R, G, and B pixels, μ_R , μ_G , and μ_B , respectively, versus image plane photon flux. Fig. 1(b) presents temporal noise power and fixed-pattern noise (FPN) power curves versus the mean photo-signal. Temporal noise, σ_{temp} , represents the variations in the pixel signal under constant illumination, and FPN, σ_{FPN} , represents the variations in the mean signal value among uniformly illuminated pixels [11], [12]. The former curve is called the photon-transfer curve (PTC) [13]. Since the only difference between R, G, and B pixels is the color filter, the curves are similar for all color channels.

Fig. 2 presents the temporal SNR, SNR_{temp} , and the total SNR, SNR_{tot} , curves versus the mean signal. SNR_{temp} is the ratio μ/σ_{temp} , and SNR_{tot} is the ratio $\mu/\sqrt{\sigma_{\text{temp}}^2 + \sigma_{\text{FPN}}^2}$, where both quantities are expressed in decibels (dB). The signal level when $\text{SNR}_{\text{tot}} = 1 = 0$ dB is marked by “SNR1.” The maximum signal level that the sensor can reach with a specific configuration file is marked by “ S_{sat} .” The dips in the SNR curves are caused by the two transitions. The first, T_{12} , is the T_1-T_2 transition, and the second, T_{23} , is the T_2-T_3 transition. The sensor DR (in dB), $\text{DR}_{\text{sensor}}$, equals $20\log_{10}(S_{\text{sat}}/\text{SNR1})$. More on SNR curves of image sensors

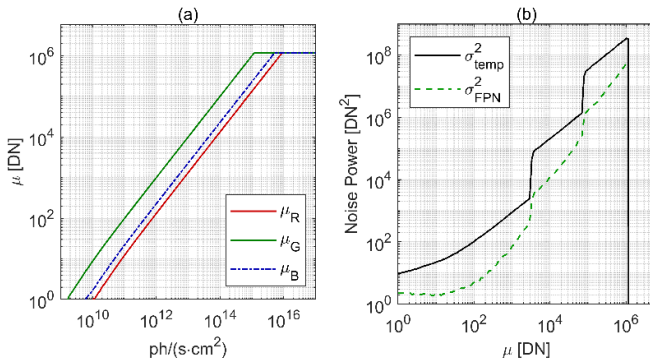


Fig. 1. Simulated signal and noise properties of an image sensor in the 3-EXP HDR mode. (a) Mean signal of R , G , and B pixels versus image plane photon flux. (b) Temporal noise and FPN power versus mean signal. The former curve is the PTC.

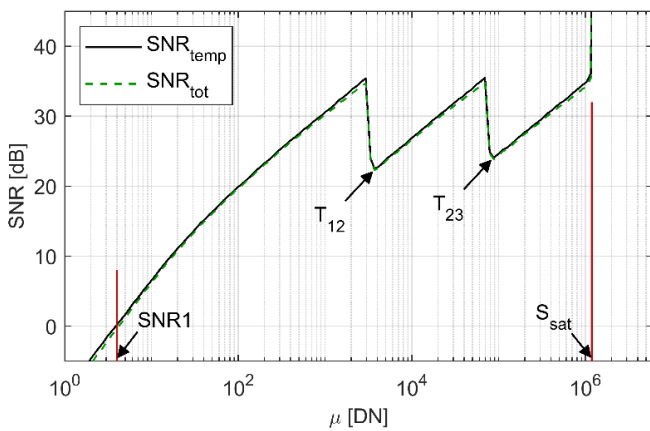


Fig. 2. Simulated temporal and total SNR curves. SNR_1 marks the signal level at which signal and noise are equal, that is, $SNR_{tot} = 0$ dB. S_{sat} is the maximum signal level that can be reached. T_{12} and T_{23} point at the SNR drops in the transition regions of the 3-EXP HDR response.

in the multi-EXP HDR mode can be found in works that were published by Yang and El Gamal [14], Spivak et al. [15], and others.

B. Proposed HDR Linearity Metric

This work proposes a linearity metric that is based on the relative channel response since a setup to produce the curves in Fig. 1(a) is very difficult to implement for image sensors that are activated in an HDR mode.

Ideally, mean photo-signals of R , G , and B pixels should be proportional to the image plane irradiance of an illuminant with a fixed spectral power distribution in the entire DR, excluding signal levels that are close to SNR_1 and S_{sat} . They do not increase at the same rate with image plane irradiance because the quantum efficiency (QE) of R , G , and B pixels is not similar. Mean photo-signal ratios should be constant, therefore, if $\mu_1(n)$ and $\mu_2(n)$ represent the mean photo-signal of two color channels, P_1 and P_2 , respectively, at sampling point n , the ratio is expressed as

$$\mu_1(n)/\mu_2(n) = K_{12} \quad (1)$$

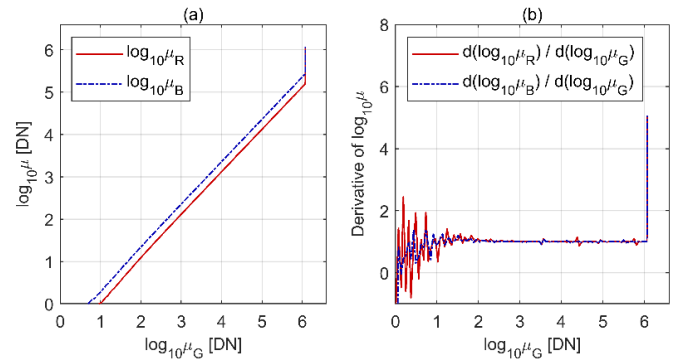


Fig. 3. (a) \log_{10} of μ_R and μ_B versus \log_{10} of μ_G at the same light level. (b) Derivatives of the curves in (a), which ideally should equal be to 1 across the entire sensor DR, excluding signal levels that close to SNR_1 or S_{sat} .

where K_{12} is a constant. By using the properties of the logarithm, (1) can be written as

$$\log_{10}(\mu_1(n)) - \log_{10}(\mu_2(n)) = \log_{10}(K_{12}). \quad (2)$$

For an ideal image sensor, (2) should hold for all sample points $n = 1, 2, \dots, N$. For example, if we measure the response at sampling point $n + 1$, we get

$$\log_{10}(\mu_1(n+1)) - \log_{10}(\mu_2(n+1)) = \log_{10}(K_{12}). \quad (3)$$

Because (2) and (3) are both equal to $\log_{10}(K_{12})$, we can set the left-handed side equal to one another and re-arrange as shown in (4). This equation, which is a one-sided derivative expression, forms the basis of this analysis

$$\frac{\log_{10}(\mu_1(n+1)) - \log_{10}(\mu_1(n))}{\log_{10}(\mu_2(n+1)) - \log_{10}(\mu_2(n))} = 1. \quad (4)$$

The result is advantageous because it is independent of the actual mean photo-signal ratio and the absolute or relative image plane irradiance. Deviation from "1" indicates deviation from linearity. In the case of monochrome sensors or applications, such as imaging in invisible bands, the same method can be applied, where the response of the single channel in the HDR mode can be compared to its response with an attenuation filter when the illumination is kept constant.

C. Simulation Results

Fig. 3(a) presents \log_{10} curves of the simulated mean photo-signals from Section A. Fig. 3(b) presents the corresponding derivative curves, that is, the curves that were obtained after the operation in (4) is applied to the data in Fig. 3(a). As expected, deviation from linearity is high at signal levels that are very low or close to saturation.

To demonstrate results with a nonlinear HDR response, the script that combines data from the T_1-T_3 signals to produce an HDR response was modified to introduce nonlinearity. Fig. 4(a) presents mean signal curves versus image plane photon flux, and Fig. 4(b) presents SNR curves with the nonlinear HDR combination. Fig. 4(a) shows that deviation from linearity starts and ends at signal levels of about 4000 DN and 100 000 DN, respectively, which correspond to T_{12} and

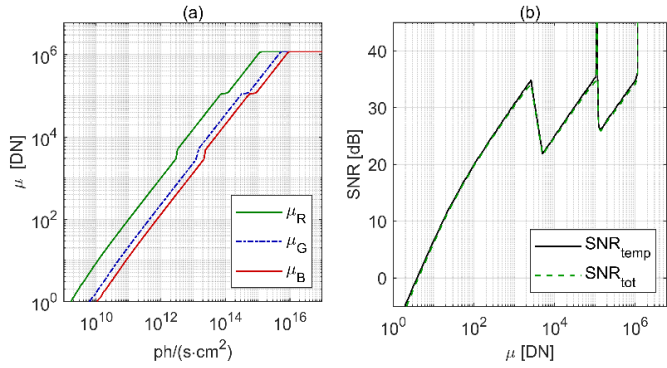


Fig. 4. Simulation results with the nonlinear HDR response. (a) Mean signal of the three color channels versus image plane photon flux and (b) SNR curves. Distortion can be observed around the T_{12} and T_{23} regions.

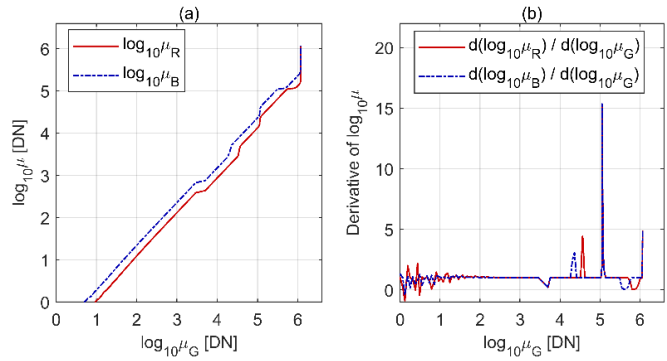


Fig. 5. Evaluation of the simulated nonlinear HDR response with the proposed linearity metric. (a) Relative response curves and (b) their derivatives. Deviation from linearity in (a) and abrupt changes in (b) occur when the signal level of at least one of the color channels is around T_{12} or T_{23} .

T_{23} . SNR curves in Fig. 4(b) show distortion around these signal levels, which are more evident when compared to the curves in Fig. 2.

The simulated nonlinear HDR response was then evaluated using the proposed HDR linearity metric. Fig. 5(a) presents the relative response curves; they show deviation from linearity where the signal level of at least one color channel is around T_{12} or T_{23} . Fig. 5(b) presents the derivatives of these curves, which demonstrate an abrupt deviation from “1” at these signal levels. Simulation results prove that the proposed method detects signal regions where the HDR response exhibits nonlinearity.

III. EXPERIMENTAL RESULTS

Experimental work was done with a camera module with a 1 MP color CIS for automotive applications. The sensor was activated in the 3-EXP HDR mode with two configuration files: C1, the default configuration file that was properly tuned, and C2, a configuration file that was modified to produce a nonlinear response, similar to the example in Section II-C.

To account for the dark signal, there are pixels at the periphery of the image sensor array that are blocked from light. These pixels, which are identical to the pixels in the imaging array, are operated with the same configuration file.

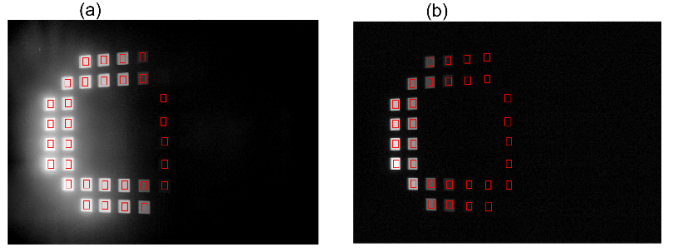


Fig. 6. Images of the transmissive test chart that were captured when the power of the LED panel behind the chart was set to (a) 100% and (b) 0.4%. Data from pixels in the marked 36×26 pixel regions were used to extract signal and noise properties of the 1 MP image sensor.

Their signals are used to estimate the dark signal in each frame, and this value is subtracted from the total signal of all pixels in the imaging array. After dark signal subtraction, white balance was applied through amplification of the signals of the R and B channels by the use of digital gain, where gain levels were adjusted with the C1 configuration file until mean signals of all color channels in neutral, that is, grayscale, regions of the scene were equal. The gains were then kept unchanged during image capture with both configuration files.

Sections A and B present results from measurements that were done in a controlled laboratory environment with an HDR test chart to construct the SNR curve, and with a continuous variable neutral density (ND) filter to implement the proposed linearity metric, respectively. In general, a single setup can be used for both purposes. This had to be divided in this work due to spectral variations in the patch transmission spectrum in the test chart, which made the data unusable for the proposed linearity metric, and due to nonnegligible signal gradients in the ND filter images, which increased FPN and prevented use of the data for the construction of a reliable SNR_{tot} curve. Section C presents results from images that were captured outdoors with natural light to correlate between the proposed linearity metric and end-user image quality.

A. SNR Curves in the HDR Mode

A setup with a transmissive 36-patch 150-dB test chart that was placed on a light-emitting diode (LED) panel was used to construct the SNR curve of the 1 MP sensor. The 30-frame image sets in raw 20-bit data format were captured with two light levels with each configuration file. A single light level was insufficient because, although the DR of the chart was greater than the sensor DR, the DR of the captured images did not exceed 100 dB due to flare inside the camera module. Fig. 6(a) and (b) presents the two images that were captured when the LED power was set to 100% and 0.4%, respectively. Pixel signals from the 36×26 pixel regions that are marked in red were analyzed in MATLAB to extract signal and noise properties. The Noise standard in IEEE P2020 [11], [12] describes the procedure that was used to process the test chart image data.

The Bayer CFA pattern has alternating rows with G -and- R and G -and- B pixels. Green pixels in G -and- R rows are called here Gr pixels, and green pixels in the G -and- B rows are called here Gb pixels. Fig. 7 presents SNR curves of the Gr

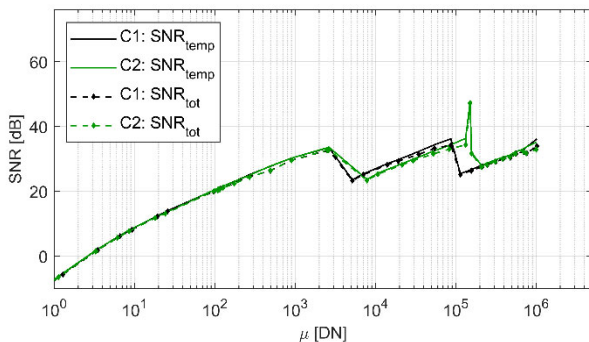


Fig. 7. SNR curves of the Gr channel that were constructed from analysis of the test chart image sets which were captured with configuration files *C1* and *C2*.

channel that were obtained from the analysis of Gr pixel data in the marked regions in the 30-frame image sets. Results are in good agreement with simulation results in Figs. 2 and 4(b). It was not possible to evaluate linearity with the proposed relative-response metric with this target because of differences in spectral transmission among the patches.

B. Linearity Evaluation With the Proposed Metric

The setup that was used to collect data to evaluate photo-response linearity with the proposed metric was based on a radial continuous variable ND filter which was placed in front of an opening of an integrating sphere with halogen light illumination. With this target, a light transmission gradient is achieved by a gradual increase in the thickness of a metal film that was deposited on the glass substrate. Since the same metal is used, there is no change in spectral transmission. The target did not include anti-reflective coating as this coating can affect the uniformity of the spectral transmission curve. The optical density of the metal-on-glass coating in the coated three-quarter circle area varied between 0.04–4.0. The filter was slightly tilted during image capture to reduce reflection artifacts.

Image sets of the variable ND filter target were captured with the two configuration files at two light levels, *L1* for low signal levels and *L2* for high signal levels up to saturation, where each set included 30 frames that were saved in a raw 20-bit data format. Fig. 8 presents 30-frame average images of the target. The images were averaged in order to minimize the effect of temporal noise and highlight variations in mean signal level. While the *C1* images in Fig. 8(a) and (b) appear grayscale, color artifacts are observed in the *C2* images in Fig. 8(c) and (d). To examine the root cause of these artifacts, signal and noise parameters were calculated in small and relatively uniform 20 × 20 pixel regions in the images, as shown in Fig. 8(e) and (f). The arrows point to regions where there is a color artifact or discontinuity in raw signal levels and indicate the signal level of the Gr channel there after dark signal subtraction.

Fig. 9 presents results from the analysis of Gr pixel data in the marked regions in the 30-frame image sets of the variable ND filter. SNR_{temp} curves in Fig. 9(a) are in agreement with the curves in Fig. 7. However, SNR_{tot} curves in the same

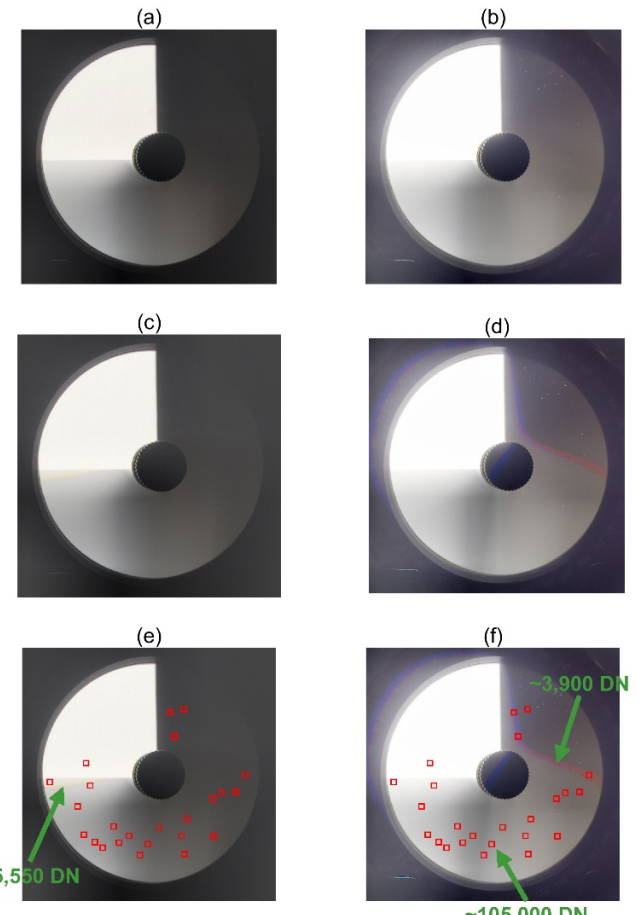


Fig. 8. Images of a back-illuminated continuous variable ND filter, where light level and configuration file are as follows: (a) *C1* and *L1*, (b) *C2* and *L2*, (c) *C2* and *L1*, and (d) *C2* and *L2*. Images (e) and (f) are the same as (c) and (d), respectively, but include markings for the 20 × 20 pixel regions that were selected for data analysis. The arrows point to regions where there is a color artifact or some discontinuity in the raw signal level and present the Gr signal level after dark signal subtraction at these locations.

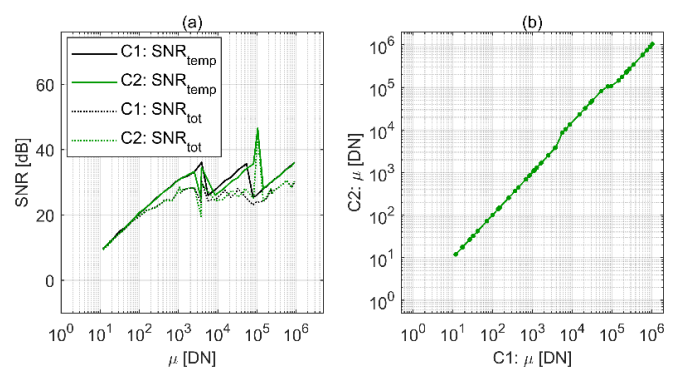


Fig. 9. Results from analysis of Gr pixel data in the marked regions in the continuous variable ND filter image sets. (a) SNR_{temp} and SNR_{tot} curves and (b) *C2* versus *C1* signal values in the same pixel regions.

plot indicate high FPN. This is expected because the gradual change in target transmission creates low-frequency structural noise in the images, which is interpreted as FPN. Fig. 9(b) presents a curve of the *C2* versus *C1* mean Gr signal after dark signal subtraction. Since the sensor photo-response is

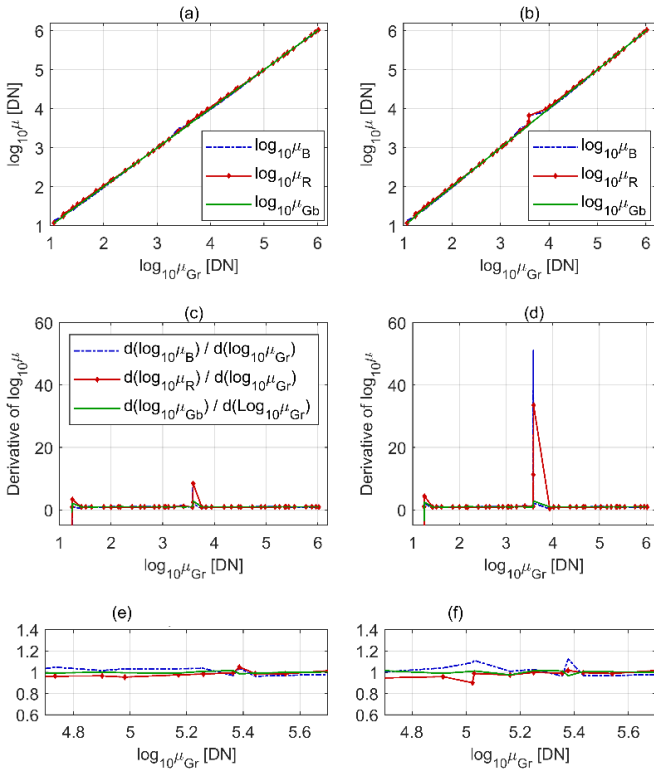


Fig. 10. Relative response curves with (a) C1 and (b) C2. Nonlinearity is clearly observed with C2 when \log_{10} of the mean Gr signal is around 3.6. Derivative curves with (c) C1 and (d) C2. The same curves with C1 and C2 at signal levels around 100 000 DN are shown in plots (e) and (f), respectively. The plots indicate that deviation from linearity is greater with C2 and that the response is not perfectly linear with C1.

expected to have high linearity with the C1 configuration (there are imperfections also with C1, as shown later), the curve indicates that there is a deviation from linearity with C2 at signal levels between 3750 and 5700 DN and between 79 000 and 145 000 DN. This is in agreement with the simulation results in Fig. 4(b).

Fig. 10(a) and (b) presents \log_{10} response curves (after dark signal subtraction) relative to the Gr channel with configuration files C1 and C2, respectively. Nonlinearity is clearly observed in Fig. 10(b) around the T_{12} signal level. Fig. 10(c) and (d) shows the derivatives of the curves in plots (a) and (b), respectively. Fig. 10(c) shows that there is a small deviation from linearity even with C1 around the T_{12} signal level, that is, when $\log_{10}(\mu_{Gr}) \approx 3.6$. Fig. 10(d) shows a much higher deviation from linearity with C2 around the same signal level. Fig. 10(e) and (f) shows the zoomed-in view to signal levels around 100 000 DN in plots Fig. 10(c) and (d), respectively. They show a deviation from 1, which is higher than C2. These results demonstrate the high sensitivity of the proposed metric to deviation from linearity. They reveal imperfections in the photo-response with the optimized configuration file, C1.

C. Outdoor Scenes

Images of an outdoor scene were captured with the two configuration files. Fig. 11(a) and (b) presents the C1 and C2

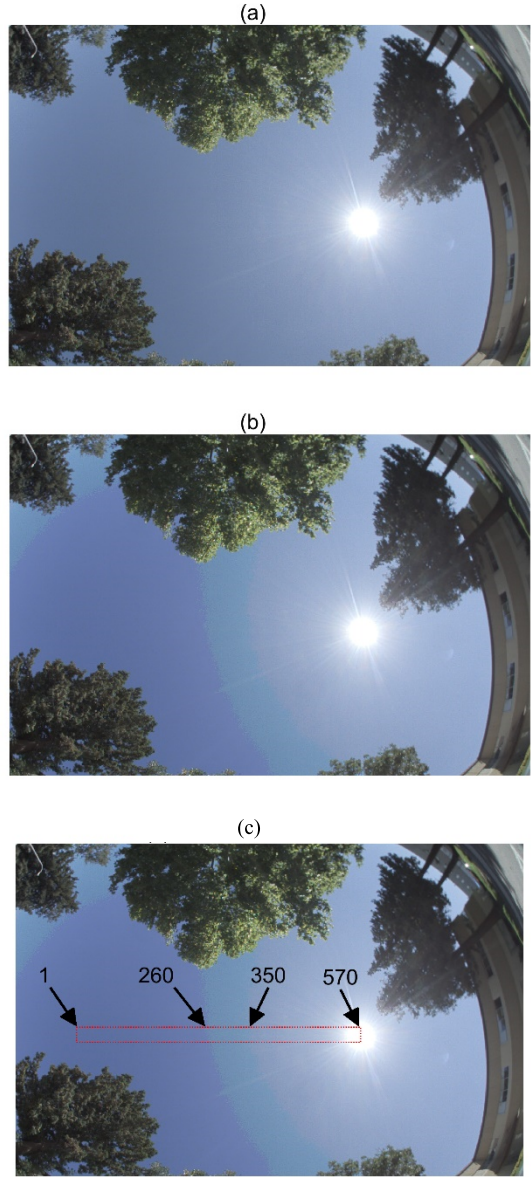


Fig. 11. Color-processed outdoor images that were captured with configuration files (a) C1 and (b) C2. Color artifacts can be observed in the sky in (b). (c) Column numbers in the pixel region that was used for data analysis.

images after color processing in the DevWare pipeline [16]. Color artifacts can be observed in the C2 image. To study the mechanism that resulted in color artifacts, mean signal levels of all color channels were evaluated in a narrow rectangular pixel region that covers areas with color artifacts in the C2 image, as shown in Fig. 11(c). Column numbers are marked in the image.

Fig. 12(a) and (b) presents mean column signal levels of raw image data after dark signal subtraction in the marked region of the images in Fig. 11(a) and (b), respectively. Mean signals of the R and B channels include the digital gains that were applied for white balance. The plots show that all signals are saturated in the sun region in the image. Mean signal values gradually decrease with distance from the sun, however, while Fig. 12(a) shows a smooth transition in the C1

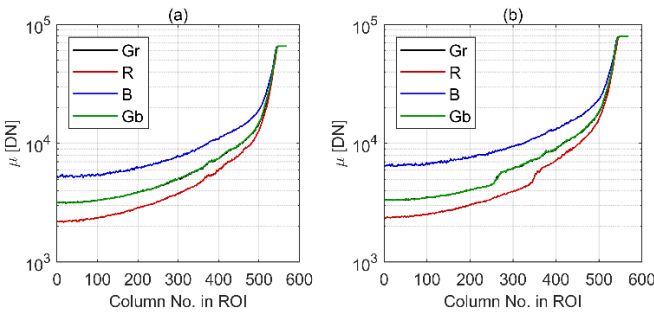


Fig. 12. Mean column raw signal level of the four color channels in the marked region in the sky in (a) C1 and (b) C2 images. Abrupt changes in the curves of the R and G color channels in (b) manifest in color artifacts in the corresponding color-processed images.

image, Fig. 12(b) shows abrupt changes in the R and G color channels in the C2 image. These abrupt changes manifest in color artifacts. The color of the sky is almost neutral close to the sun, in column numbers above 350 and until the beginning of saturation. The abrupt drop in the mean R signal around column 350, leaves excess blue and green, which appears as a green band in column numbers 260–350. Then, the abrupt drop in mean Gr and Gb signals at column 260 leaves the image with excess blue. Signal levels of the R and G channels in locations where the abrupt changes in mean signals occur match the T_{12} transition.

IV. LINEARITY AND COLOR ARTIFACTS

Sections III-B and III-C demonstrated correlation between nonlinearity in the HDR response of color image sensors and objectionable color artifacts in the image after color reproduction. Color artifacts are unwanted in viewing applications and can misguide machine vision systems, as they may use color for object detection, segmentation, and classification [17], [18]. Section A presents an approach to the quantification of color properties, and Section B discusses the correlation between deviation from linearity and color artifacts.

A. Color Properties Quantification

Color properties of the images that were presented in Section III were evaluated by converting raw signal values of the color channels in the selected pixel regions into $L^*a^*b^*$ color space quantities. This was done in two stages [19]: 1) conversion from linear RGB to XYZ color space and 2) conversion from XYZ to $L^*a^*b^*$ color space. To convert the linear RGB raw image data into XYZ, Gr and Gb signal values were averaged for each pixel region. Afterward, the linear RGB signals were normalized in each region, and XYZ values were calculated as follows:

$$\begin{bmatrix} X \\ Y \\ Z \end{bmatrix} = [M] \begin{bmatrix} R \\ G \\ B \end{bmatrix} \quad (5)$$

where M is the sRGB transformation matrix with the following coefficients [20]:

$$M = \begin{bmatrix} 0.4124 & 0.3576 & 0.1805 \\ 0.2126 & 0.7152 & 0.0722 \\ 0.0193 & 0.1192 & 0.9505 \end{bmatrix}. \quad (6)$$

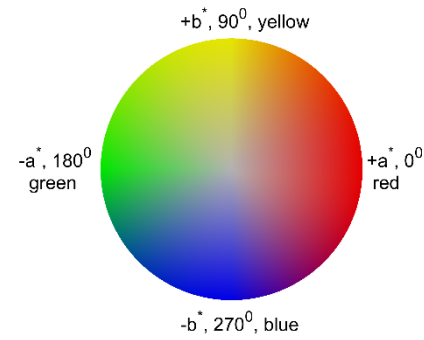


Fig. 13. $L^*a^*b^*$ color space. The radius, which is correlated with colorfulness, is the chroma, and the angle is the hue.

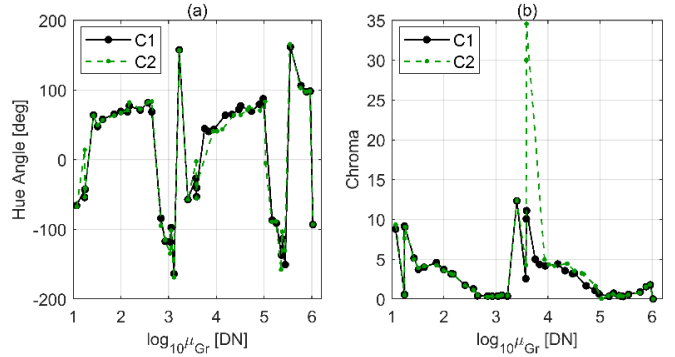


Fig. 14. Color properties of the continuous variable ND filter images. (a) Hue angle and (b) chroma. With C2, when $\log_{10}(\mu_{Gr}) \approx 3.6$, the chroma is high, and the hue angle is about 0° , which is red.

For XYZ to $L^*a^*b^*$ conversion, the standard 2° observer with a D65 illuminant XYZ tristimulus values was used for white reference, that is, $X_r = 95.047$, $Y_r = 100$, and $Z_r = 108.883$.

Fig. 13 presents a diagram of the CIE $L^*a^*b^*$ color space; it was prepared using the cielabplot script in the color toolbox of [21]. The radius is the chroma, C^* , which is correlated with colorfulness. Therefore, in the center, where the color is neutral or grayscale, chroma is 0. The angle is correlated with hue, for example, 0° represents red.

Chroma is calculated as follows:

$$C^* = \sqrt{a^{*2} + b^{*2}} \quad (7)$$

and hue, h , is calculated as

$$h = \tan^{-1}(b^*/a^*). \quad (8)$$

B. Correlation With Nonlinearity

Fig. 14(a) and (b) presents the hue angle and chroma, respectively, of the selected regions in the continuous variable ND filter images. Fig. 14(a) shows that the hue angle is similar with both configuration files at all signal levels, excluding small differences when the mean Gr signal is in the range of 4000–10 000 DN. Fig. 14(b) shows that C^* is rather low, excluding around $\log_{10}(\mu_{Gr}) \approx 3.6$ with C2. The low chroma values correlate with image regions where the filter appears gray, that is, color-neutral. With C2, when $\log_{10}(\mu_{Gr}) \approx 3.6$,

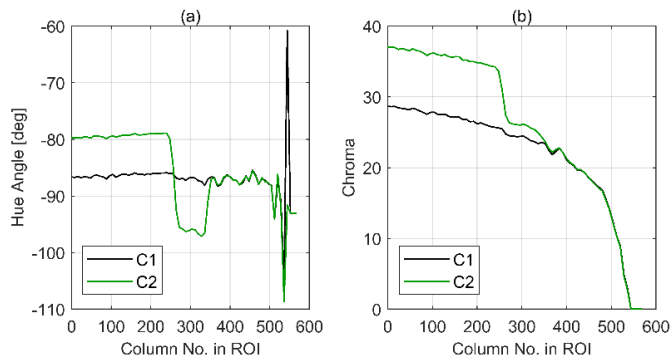


Fig. 15. Color properties of the marked region in the outdoor images. (a) Hue angle. (b) Chroma.

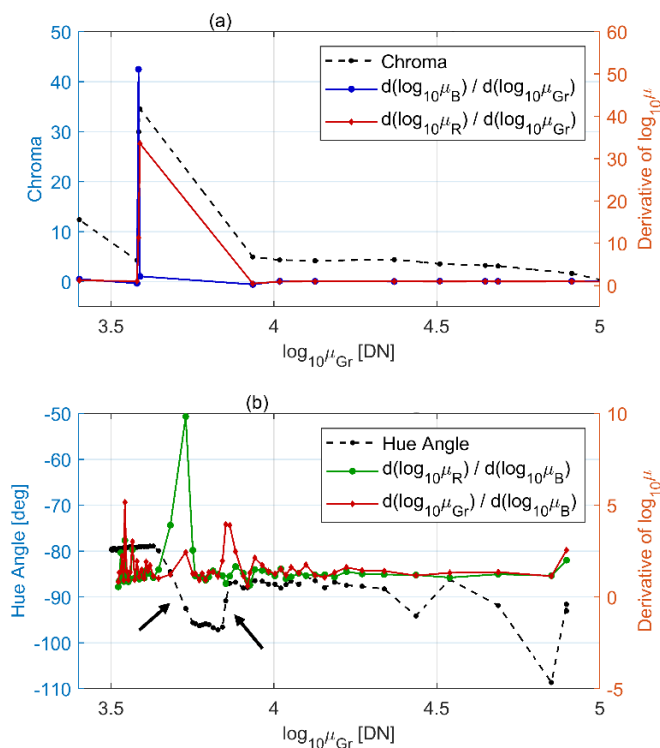


Fig. 16. Correlation between the proposed HDR linearity metric and color properties of laboratory and outdoor images that were captured with C2. (a) Chroma and log-signal derivatives of the variable ND filter image. (b) Hue and log-signal derivative of the outdoor sky image. The arrows point to regions where the division from “1” in one of the log-signal derivative curves correlates with an abrupt change in the hue angle.

the hue angle is about 0° , which is red. This is in agreement with the color of the image in that region.

Fig. 15(a) and (b) presents hue angle and chroma, respectively, in the marked region in the outdoor images. With C1, the hue angle is close to -87° , which is blueish, in the entire region until saturation where the white color of the sun results in 0 chroma in the image. With C2, the hue angle starts around -79° , which is purplish-blue, then changes to about -96° , which is greenish blue. Afterward, the hue angle with both configuration files is similar. All this is in agreement with the color in the two outdoor images.

Fig. 16 summarizes results for the same signal range from laboratory and outdoor images that were captured with C2.

Fig. 16(a) shows chroma and log-signal derivative curves from selected regions in the variable ND filter image. An abrupt substantial deviation from “1” in the derivative curves occurs at the same signal level where there is an abrupt increase in chroma in the image of the grayscale target. Fig. 16(b) shows the hue and log-signal derivative curves that were obtained from selected regions in the outdoor sky image. The derivatives in this plot were calculated relative to the B channel because it is the only channel with a smooth change in mean signal level. Arrows in the plot point to a correlation between sudden changes in hue in columns 250 and 360 in the marked region in the image in Fig. 11(c) and abrupt changes in the derivatives.

V. CONCLUSION

This work presented a method for the evaluation of the linearity of image sensors in the HDR mode. The method is based on the relative derivatives of the logarithm of the signals of different color channels. It is advantageous because it does not require a high-precision HDR light source, and because the ideal value, “1,” is independent of actual channel response ratios. Results from the simulation of an image sensor in linear and nonlinear 3-EXP HDR modes and from analysis of images that were captured with a 1 MP automotive image sensor that was activated in these modes showed that the method is sensitive to deviation from linearity, including minor deviations around transition regions of an image sensor in normal operation. Furthermore, this work demonstrated a correlation between deviation from linearity and color artifacts in color cameras.

ACKNOWLEDGMENT

The authors would like to thank Shaheen Amanullah for useful discussions and data. They would also like to thank Paul Romanczyk for helpful feedback on the metric.

REFERENCES

- [1] F. Wang and A. J. P. Theuwissen, “Pixel optimizations and digital calibration methods of a CMOS image sensor targeting high linearity,” *IEEE Trans. Circuits Syst. I, Reg. Papers*, vol. 66, no. 3, pp. 930–940, Mar. 2019.
- [2] Standard for Characterization of Image Sensors and Cameras, EMVA Standard 1288, European Machine Vision Association, 2021.
- [3] J. Stumpfel, A. Jones, A. Wenger, C. Tchou, T. Hawkins, and P. Debevec, “Direct HDR capture of the sun and sky,” in *Proc. ACM SIGGRAPH Courses*, 2006, pp. 1–5.
- [4] I. Takayanagi and R. Kuroda, “HDR CMOS image sensors for automotive applications,” *IEEE Trans. Electron Devices*, vol. 69, no. 6, pp. 2815–2823, Jun. 2022.
- [5] R. J. Palum, “Image sampling with the Bayer color filter array,” in *Proc. Image Capture Syst. Conf. (PICTS)*, 2001, pp. 239–245.
- [6] N. V. Loukianova et al., “Leakage current modeling of test structures for characterization of dark current in CMOS image sensors,” *IEEE Trans. Electron Devices*, vol. 50, no. 1, pp. 77–83, Jan. 2003.
- [7] B. Fowler, D. McGrath, and P. Bartkovjak, “Read noise distribution modeling for CMOS image sensors,” in *Proc. Int. Image Sensor Workshop*, 2013, pp. 1–4.
- [8] B. Pain, T. Cunningham, B. Hancock, C. Wrigley, and C. Sun, “Excess noise and dark current mechanisms in CMOS Imagers,” in *Proc. Int. Image Sensor Workshop (IISW)*, 2005, pp. 145–148.
- [9] H. Tian, B. Fowler, and A. E. Gamal, “Analysis of temporal noise in CMOS photodiode active pixel sensor,” *IEEE J. Solid-State Circuits*, vol. 36, no. 1, pp. 92–101, Jan. 2001.

- [10] B. C. Kim, J. Jeon, and H. Shin, "Temporal noise analysis and reduction method in CMOS image sensor readout circuit," *IEEE Trans. Electron Devices*, vol. 56, no. 11, pp. 2489–2495, Nov. 2009.
- [11] *IEEE Draft Standard for Automotive System Image Quality*, Standard IEEE P2020/D3, 2022.
- [12] O. Skorka and P. Romanczyk, "A review of IEEE P2020 noise metrics," in *Proc. IS&T Int. Symp. Electron. Imag.*, 2022, pp. 109-1–109-6.
- [13] J. R. Janesick, *Photon Transfer DN to Lambda*. Bellingham, WA, USA: SPIE, 2007.
- [14] D. X. D. Yang and A. E. Gamal, "Comparative analysis of SNR for image sensors with enhanced dynamic range," *Proc. SPIE*, vol. 3649, pp. 197–211, Apr. 1999.
- [15] A. Spivak, A. Belenky, A. Fish, and O. Yadid-Pecht, "Wide-dynamic-range CMOS image sensors—Comparative performance analysis," *IEEE Trans. Electron Devices*, vol. 56, no. 11, pp. 2446–2461, Nov. 2009.
- [16] Onsemi. *DevWare—DevSuite—Confluence*. Accessed: Feb. 14, 2023. [Online]. Available: https://onsemi.sharepoint.com/teams/isg-competitor_analysis
- [17] R. Bergman and H. Nachlieli, "Perceptual segmentation: Combining image segmentation with object tagging," *IEEE Trans. Image Process.*, vol. 20, no. 6, pp. 1668–1681, Jun. 2011.
- [18] Y. Yang, H. Luo, H. Xu, and F. Wu, "Towards real-time traffic sign detection and classification," *IEEE Trans. Intell. Transp. Syst.*, vol. 17, no. 7, pp. 2022–2031, Oct. 2016.
- [19] B. J. Lindbloom. (2022). *Bruce Lindbloom.com*. Accessed: Sep. 13, 2022. [Online]. Available: <http://www.brucelindbloom.com/index.html?ColorCalculator.html>
- [20] *Amendment 1*, Standard IEC 61966-2-1:1999, 2003.
- [21] S. Westland, *Computational Colour Science using MATLAB 2e*. Chichester, U.K.: Wiley, 2023.
- [22] J. C. Dunlap, M. M. Blouke, E. Bodegom, and R. Widenhorn, "Interpreting activation energies in digital image sensors," *IEEE Trans. Electron Devices*, vol. 63, no. 1, pp. 26–31, Jan. 2016.

Orit Skorka (Member, IEEE) received the B.Sc. degree in electrical and computer engineering from the Ben Gurion University of the Negev, Beersheba, Israel, in 2001, the M.Sc. degree in electrical and computer engineering from the Technion IIT, Haifa, Israel, in 2004, and the Ph.D. degree from the University of Alberta, Edmonton, AB, Canada, in 2011.

She joined onsemi, Santa Clara, CA, USA, in 2013, where she is with the Technology Research and Development Team, Intelligent Sensing Group, working on pixel characterization and sensor image quality.

Barry Vanhoff received the Ph.D. degree in electrical engineering from Washington State University, Pullman, WA, USA, in 1996.

He was a Research Associate with the Department of Oceanic and Atmospheric Sciences, Oregon State University, Corvallis, OR, USA. He has been with a Camera Characterization Engineer and the Design Manager with onsemi (previously Aptina), Corvallis, OR, USA, since 2011.

Rujul Desai received the M.Sc. degree in imaging science from the Rochester Institute of Technology, Rochester, NY, USA, in 2021.

He has been a Characterization Engineer with the Intelligent Sensing Group, onsemi, Santa Clara, CA, USA, since 2021.

Radu Ispasoiu received the Ph.D. degree in physics with a focus on semiconductor optoelectronic device study from the University of Oxford, Oxford, U.K., in 1996.

He is the Director of Pixel Research and Development, Intelligent Sensing Group, onsemi, Santa Clara, CA, USA. He has held engineering management and lead research and development positions in the Silicon Valley optoelectronics technology industry for more than 20 years.